



Fabrication of a Novel p–n Heterojunction BiOCl/Ag₆Si₂O₇ Nanocomposite as a Highly Efficient and Stable Visible Light Driven Photocatalyst

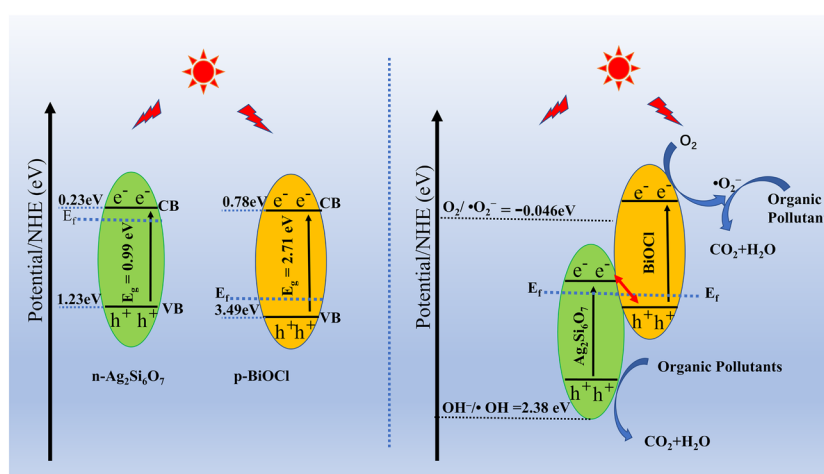
Jibo Qin¹ · Nan Chen¹ · Chuanping Feng¹ · Huiping Chen¹ · Zhengyuan Feng¹ · Yu Gao² · Zhenya Zhang³

Received: 17 September 2018 / Accepted: 4 December 2018
© Springer Science+Business Media, LLC, part of Springer Nature 2018

Abstract

Herein, a visible-light-active BiOCl/Ag₆Si₂O₇ nanocomposite with a strong interfacial interaction p–n heterojunction structure was fabricated via a simple deposition–precipitation method and subsequently investigated as a novel photocatalyst for the first time. The structure, morphology, and optical properties of the prepared samples were thoroughly characterized by field-emission scanning electron microscopy, transmission electron microscopy (TEM), high-resolution TEM, X-ray diffraction, diffuse reflectance spectroscopy, X-ray photoelectron spectroscopy, and Fourier transform infrared spectroscopy. The photocatalytic performance was evaluated by monitoring the degradation of methyl orange (MO) and phenol and the photocurrent generated under visible-light irradiation. The BiOCl/Ag₆Si₂O₇ photocatalyst increased significantly its photocatalytic performance compared to the pristine BiOCl and Ag₆Si₂O₇ materials. This enhancement could be ascribed to the strong visible light absorption and the effective separation of the photogenerated electrons (e⁻) and holes (h⁺) by the internal electrostatic field generated at the junction region. In addition, BiOCl/Ag₆Si₂O₇ showed stable photocurrent over long times and cyclic degradation of MO, thereby demonstrating potential applications in the field of environmental remediation.

Graphical abstract



Z-scheme photocatalytic mechanism of the of the BiOCl/Ag₆Si₂O₇ photocatalyst.

Keywords BiOCl/Ag₆Si₂O₇ nanocomposite · Heterojunction structure · Visible light · Phenol and MO degradation · Stability

Extended author information available on the last page of the article

1 Introduction

Photocatalysis using semiconductors has been recognized as an effective method for mitigating environmental pollution and energy shortage problems owing to the superior solar energy capture and utilization abilities of these materials [1–5]. Numerous semiconductors (e.g., $g\text{-C}_3\text{N}_4$, Bi_2WO_6 , CeO_2 , and AgVO_3) have been recently used in a number of processes, including organic pollutant degradation to H_2O and CO_2 [6, 7] and water splitting to H_2 and O_2 [8]. However, the photocatalytic efficiency of the existing photocatalysts is currently limited by many factors, including the high recombination rate of the photogenerated e^- – h^+ pairs, the narrow light absorption range, and the low photocatalytic efficiency [9]. These issues have been widely tackled by researchers by using new methods such as metal doping [10–12], noble metal loading [13] and preparation of composite photocatalysts with fine heterostructure [14]. Among these methods, the preparation of photocatalysts with heterojunctions has been considered to be the most effective and feasible approach [15, 16] since electron–hole (e^- – h^+) pair recombination is effectively suppressed in the presence of heterojunctions. However, highly efficient heterojunction systems are very difficult to prepare since the fine heterojunction are required combine wide light absorption ranges with high photogenerated charge–carrier separation rates. Coupling of two semiconductor photocatalysts require them to present a well-matched band structure and a suitable molar ratio. Therefore, it is urgent and crucial to prepare a coupled photocatalyst with a well-matched conduction and valence bands (CB and VB, respectively).

Bi-based compounds are currently used as photocatalysts for pollution control and environmental restoration [17]. These compounds include Bi_2O_3 [18], Bi_2WO_6 [19], BiVO_4 [20], $\text{Bi}_2\text{MnNbO}_7$ ($M = \text{Al, Sm, and Fe}$) [21], and BiOX ($X = \text{Cl, Br, and I}$) [22]. Among these photocatalysts, BiOCl has been widely used for photooxidation and disinfection of polluted wastewaters owing to its unique physical structure and high photocatalytic stability [23]. However, BiOCl has a large bandgap and therefore the excitation of the photogenerated charge carriers, which can degrade organic pollutants are carried out only under ultraviolet (UV) irradiation, thus severely limiting its practical application [24]. Therefore, constructing heterojunction structures by coupling BiOCl with other suitable semiconductors is a reasonable method to enhance its light absorption capability and photocatalytic activity. However, examples of p–n type composite heterogeneous systems containing BiOCl -based junction photocatalytic materials are scarce in the literature, with $\text{BiPO}_4/\text{BiOCl}$ [25], $\text{BiOCl}/\text{Bi}_2\text{MoO}_6$ [26], $\text{BiOCl}\text{-SrFe}_{12}\text{O}_{19}$ [27], and $\text{BiOCl}/$

C_3N_4 [28] being the only systems described. Despite having broadened light absorption ranges and improved photocatalytic activities, these catalysts are expensive, require complex preparation procedures, and present low photocatalytic efficiency towards the degradation of methyl orange (MO) or phenol. In order to overcome these drawbacks, it is necessary to combine BiOCl with other suitable semiconductors.

$\text{Ag}_6\text{Si}_2\text{O}_7$ is a typical n-type semiconductor in which the photogenerated e^- – h^+ are effectively separated by the unique internal electric field structure of this material [29]. $\text{Ag}_6\text{Si}_2\text{O}_7$ has a very narrow band gap (1.58 eV) [30] such that it absorbs light over the entire UV and Visible regions (< 740 nm) [31]. Therefore, $\text{Ag}_6\text{Si}_2\text{O}_7$ can be used as a highly efficient photosensitive modifier for improving the visible-light photocatalytic activity of wide band-gap semiconductors. To our delight, by investigating the energy levels of $\text{Ag}_6\text{Si}_2\text{O}_7$, we found that the band structures of n- $\text{Ag}_6\text{Si}_2\text{O}_7$ and p- BiOCl match well. Thus, both materials can be used to construct p–n heterojunction photocatalysts with high visible-light catalytic performance. However, to the best of our knowledge, the preparation and application of p- $\text{BiOCl}/\text{n-Ag}_6\text{Si}_2\text{O}_7$ heterojunction photocatalyst has not been reported yet.

In this study, $\text{BiOCl}/\text{Ag}_6\text{Si}_2\text{O}_7$ nanocomposites with p–n junction structure were developed by a simple deposition–precipitation method at room temperature. Various characterization techniques were used to study the structure, morphology, and optical properties of these heterojunctions. MO (as a dye model) and phenol (as representative of colorless contaminants) were used to evaluate the photocatalytic activity of the $\text{BiOCl}/\text{Ag}_6\text{Si}_2\text{O}_7$ p–n heterojunction nanocomposite under visible-light illumination. The effect of the Bi/Ag molar ratio on the photocatalytic performance and the stability of the hybrids were investigated. Besides, the intermediate products, the photodegradation mechanism, and the degradation pathways were also demonstrated and studied in detail.

2 Experimental

2.1 Materials and Methods

All reagents used were of analytical grade and were used without further purification. For the synthesis of BiOCl , 0.458 g $\text{Bi}(\text{NO}_3)_3 \cdot 5\text{H}_2\text{O}$ powder was dissolved in 25 mL of ethylene glycol to prepare a $\text{Bi}(\text{NO}_3)_3$ glycol solution, which was placed in an ultrasonic bath for 15 min to obtain a uniformly mixed solution. At the same time, a certain amount of KCl was added to 15 mL of deionized water. Then, the as-prepared KCl solution was added to the $\text{Bi}(\text{NO}_3)_3$ glycol solution. After continuous magnetic stirring for 30 min, a

white solid product was collected by filtration, washed, and dried for 12 h.

The BiOCl/Ag₆Si₂O₇ nanocomposite photocatalyst was prepared by a simple co-precipitation process at room temperature. Typically, 1 mM AgNO₃ and 1 mM BiOCl aqueous solutions were prepared by dissolving these solids in 50 mL of deionized water. Then, a Na₂SiO₃ solution (20 mL, 0.05 M) was added dropwise to the above mixed solution. After that, the solid product was collected and washed several times with deionized water. Finally, the samples were dried in an oven at 65 °C for 12 h to yield the BiOCl/Ag₆Si₂O₇ photocatalyst. A series of x BiOCl/Ag₆Si₂O₇ (with x being the molar ratio of Bi to Ag; x = 1/4, 2/1, 1/1, 1/2, and 4/1) were synthesized by using the same above method, while pure Ag₆Si₂O₇ was prepared similarly but without adding BiOCl.

2.2 Characterization

The morphology of the as-obtained samples was characterized by field emission scanning electron microscopy (FESEM, GeminiSEM500, Zeiss, Germany) and transmission electron microscopy (TEM, JEM-2100, Jeol, Japan). The phase structure and chemical composition of the photocatalysts were evaluated by X-ray diffraction (XRD, D8 Focus, Bruker, Germany) and X-ray photoelectron spectroscopy (XPS, ESCALAB 250Xi, Thermo Fisher, USA), respectively. The UV–Vis diffuse reflection spectra (DRS) of the samples were recorded on a UV–Visible-near infrared spectrophotometer (Cary 5000, Varian, USA). Fourier transform infrared spectroscopy (FTIR, Vertex 70V, Bruker, Germany) was used for analyzing the surface functional groups of the BiOCl, Ag₆Si₂O₇, and BiOCl/Ag₆Si₂O₇ samples. The photocatalytic degradation intermediates and the end products resulting from the degradation of MO were detected by a gas chromatography (GC, Agilent 7890A, Agilent Technologies, USA).

2.3 Photocatalytic Performance

The photocatalytic performance of the BiOCl, Ag₆Si₂O₇, and x BiOCl/Ag₆Si₂O₇ samples towards the photodegradation of MO (10 mg/L) and phenol (30 mg/L) were carried out under visible light illumination with an average light intensity of 40 mW/cm². At the initial stage of the photocatalytic reaction, 100 mg of photocatalyst were ultrasonically dispersed in a 300 mL glass beaker containing 100 mL of MO or phenol solutions at room temperature. Subsequently, the mixed solution was vigorously stirred in dark for 15 min to complete the adsorption–desorption balance between MO (or phenol) and the photocatalyst. Afterwards, the Xe lamp was turned on to start the photocatalytic reaction. At given intervals, 2.5 mL of the reacted liquid were quickly taken

out and filtered (0.22 μm drainage membrane) to remove the solid photocatalyst particles. Finally, the above solutions containing MO and phenol were analyzed on a UV–Vis spectrophotometer (DR6000, HACH, USA) and a high-efficiency liquid chromatograph (Agilent 1206, Agilent Technologies, USA), respectively. The degradation efficiency (%) was calculated by using the following equation:

$$\text{Degradation efficiency (\%)} = C_t/C_0 \times 100\% \quad (1)$$

where C₀ (mg/L) and C_t (mg/L) are the concentrations of the target organic solution at irradiation times 0 and t (min), respectively.

3 Results and Discussion

3.1 Characterization

3.1.1 FESEM and TEM

The surface morphology and particle size of the obtained BiOCl, Ag₆Si₂O₇, and 1/1 BiOCl/Ag₆Si₂O₇ nanocomposites were characterized by TESEM and TEM (Fig. 1). Figure 1a shows the FESEM images of pure Ag₆Si₂O₇, which consisted of regular and smooth spherical particles of 100 nm in diameter. In contrast, the BiOCl powders (Fig. 2b) exhibited an irregular and non-uniform spherical structure with a diameter of ca. 1 μm. Figure 1c, d show the FESEM and TEM images of the 1/1 BiOCl/Ag₆Si₂O₇ composite, respectively. As shown in Fig. 1c, d, Ag₆Si₂O₇ was tightly associated with BiOCl forming particles of 30 nm in diameter.

In order to further determine the existence of a heterojunction structure between BiOCl and Ag₆Si₂O₇, the 1/1 BiOCl/Ag₆Si₂O₇ nanocomposite was investigated by HRTEM. The magnified HRTEM image (Fig. 1e) clearly revealed fringes with lattice spacings of 0.264 and 0.245 nm, which could be indexed to the (1 2 4) and (0 0 3) planes of Ag₆Si₂O₇ and BiOCl, respectively. These results confirmed the existence of a BiOCl/Ag₆Si₂O₇ heterojunction. Therefore, the BiOCl/Ag₆Si₂O₇ photocatalyst could effectively inhibit recombination of the photogenerated e[−]–h⁺ pairs and greatly improve the efficiency of light capture and its utilization.

3.1.2 XRD

The crystal structures of the BiOCl, Ag₆Si₂O₇, and 1/1BiOCl/Ag₆Si₂O₇ nanocomposite catalysts were investigated by XRD at room temperature, and the results are displayed in Fig. 2. Regarding BiOCl (Fig. 2a), diffraction peaks at 2θ = 12.10, 25.90, 32.80, 33.52, 41.06, and 46.67° were clearly observed, which corresponded to the (0 0 1), (1 0 1), (1 1 0), (1 0 2), (1 1 2), and (2 0 0) planes

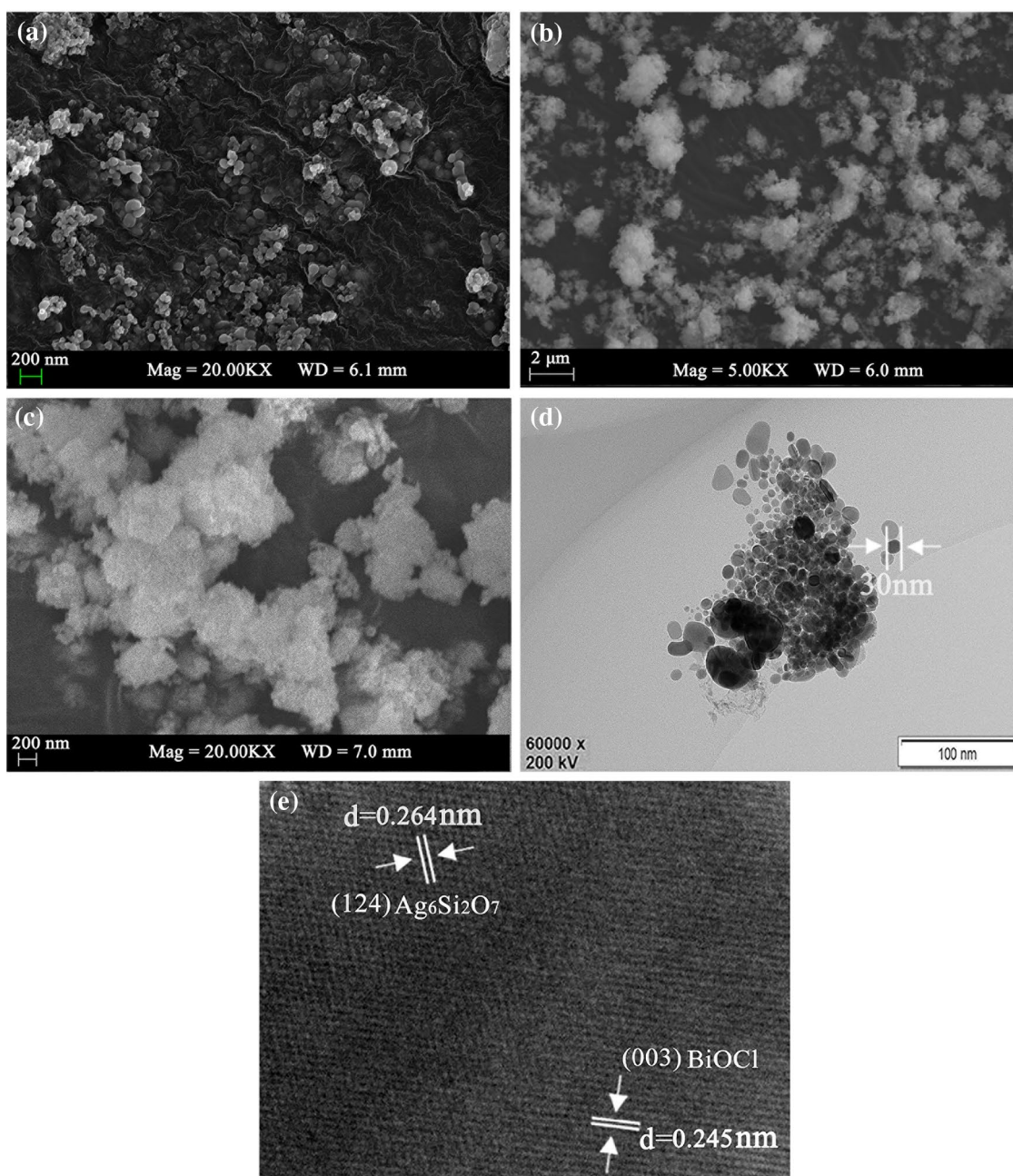


Fig. 1 FESEM images of $\text{Ag}_6\text{Si}_2\text{O}_7$ (a); BiOCl (b) and 1/1 $\text{BiOCl}/\text{Ag}_6\text{Si}_2\text{O}_7$ (c), TEM (d) and HRTEM (e) images 1/1 $\text{BiOCl}/\text{Ag}_6\text{Si}_2\text{O}_7$

of a tetragonal BiOCl phase (JCPDS 06-0249) [32]. The XRD pattern of $\text{Ag}_6\text{Si}_2\text{O}_7$ (Fig. 2b) contained one prominent peak at ca. 34.01° , characteristic of the (1 2 4) plane of the $\text{Ag}_6\text{Si}_2\text{O}_7$ phase (JCPD File No. 85-0281) [30, 33]. The diffraction pattern of the $\text{BiOCl}/\text{Ag}_6\text{Si}_2\text{O}_7$ nanocomposites (Fig. 2c) revealed the presence of intense sharp peaks, indicating that the catalysts were well-crystallized. Compared to the fresh sample, the XRD pattern of $\text{BiOCl}/\text{Ag}_6\text{Si}_2\text{O}_7$ after four reaction cycles (Fig. 2d) remained unchanged with regards to the position and intensity of the peaks, thereby

revealing good stability. In addition, no impurity peaks were found for the $\text{BiOCl}/\text{Ag}_6\text{Si}_2\text{O}_7$ heterojunction, which suggested that the photocatalyst was only composed of BiOCl and $\text{Ag}_6\text{Si}_2\text{O}_7$.

3.1.3 XPS

To further determine the chemical composition and different chemical status of the $\text{BiOCl}/\text{Ag}_6\text{Si}_2\text{O}_7$ photocatalyst, XPS analysis was conducted. The full-range XPS survey

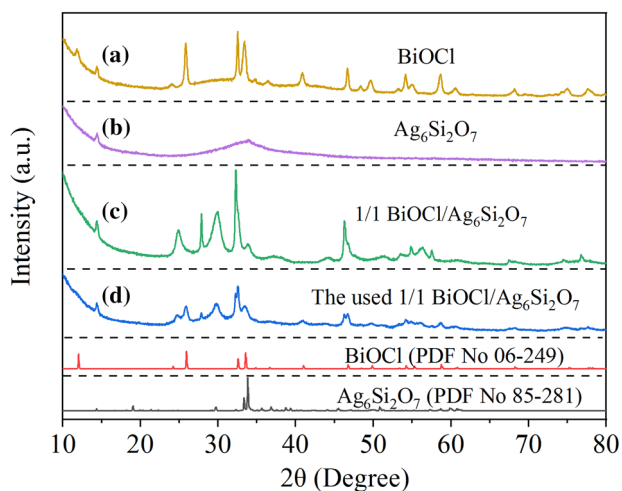


Fig. 2 XRD patterns of the BiOCl (a); Ag₆Si₂O₇ (b); 1/1 BiOCl/Ag₆Si₂O₇ (c) and used 1/1 BiOCl/Ag₆Si₂O₇ sample (d)

spectrum of BiOCl/Ag₆Si₂O₇ (Fig. 3a) revealed the presence of Bi, Cl, O, Ag and Si (the C 1s peak was ascribed to adventitious hydrocarbon from the XPS instrument itself). The high-resolution Bi 4f XPS spectrum is shown in Fig. 3b. The two peaks at 159.09 and 164.50 eV were assigned to the Bi 4f_{7/2} and Bi 4f_{5/2} transitions respectively, and were characteristics of Bi³⁺ in BiOCl [34]. As shown in Fig. 3c, two peaks at 199.80 and 198.20 eV were observed in the Cl 2p spectrum, which were ascribed to Cl 2p_{1/2} and Cl 2p_{3/2} transitions, respectively [35]. The two peaks at 374.38 and 368.37 eV (Fig. 3d) were indexed to the Ag 3d_{3/2} and Ag 3d_{5/2} transitions of Ag₆Si₂O₇, respectively [30, 33]. The XPS pattern of pure BiOCl (Fig. 3e) revealed that this sample was high purity, since it only contained Bi, O, and Cl signals.

3.1.4 DRS

UV–Vis DRS was used to explore the optical properties of the samples. As shown in Fig. 4a, Ag₆Si₂O₇ possessed a strong photo-absorption ability in the UV and visible–light regions, and this photo-absorption extended to 640 nm. In contrast, BiOCl exhibited a strong absorption only in the UV region. Coupling of BiOCl and Ag₆Si₂O₇ resulted in BiOCl/Ag₆Si₂O₇ composites having an enhanced optical absorption properties than pure BiOCl. Meanwhile, the band gap of the samples were calculated by the Kubelka–Munk expression [36]:

$$(h\nu\alpha)^{1/n} = A(h\nu - E_g) \quad (2)$$

where α is the optical absorption coefficient; $h\nu$ is the incident photonic energy (eV); A is the proportionality constant; E_g is the band gap energy (eV); and n is a factor that depends on the kind of optical transition induced by photon

absorption (i.e., 1/2 and 2 for direct and indirect transitions, respectively).

Using $n = 1/2$, the direct band gap energy of the 1/1 BiOCl/Ag₆Si₂O₇ heterostructure was estimated to be 1.87 eV (Fig. 4b), which revealed the narrow-band-gap characteristics of this photocatalyst. This value was lower than that of BiOCl (2.71 eV), thereby demonstrating that the deposition of Ag₆Si₂O₇ on BiOCl was effective in increasing the absorbance of visible light and the number of available photogenerated carriers. The Mott–Schottky curve of Ag₆Si₂O₇ was also measured without light (Fig. 4c). The linear plot showed a positive slope, revealing the n-type semiconductor nature of Ag₆Si₂O₇. The flat potential was calculated to be -0.03 eV (vs. standard calomel electrode (SCE)), which corresponded to 0.21 V (vs. normal hydrogen electrode (NHE)). N-type semiconductors are well-known for having CB 0–0.1 eV above the flat potential [37, 38]. Here, the voltage difference between the CB and the flat potential was set to 0.02 eV. Therefore, the CB of Ag₆Si₂O₇ was calculated to be 0.23 eV. Combing the above results and the band-gap values extrapolated in the DRS spectra (Fig. 4b), the VB of Ag₆Si₂O₇ was estimated to be 1.23 eV.

Thus, the corresponding band edge positions of BiOCl was calculated by using the following equation [39]:

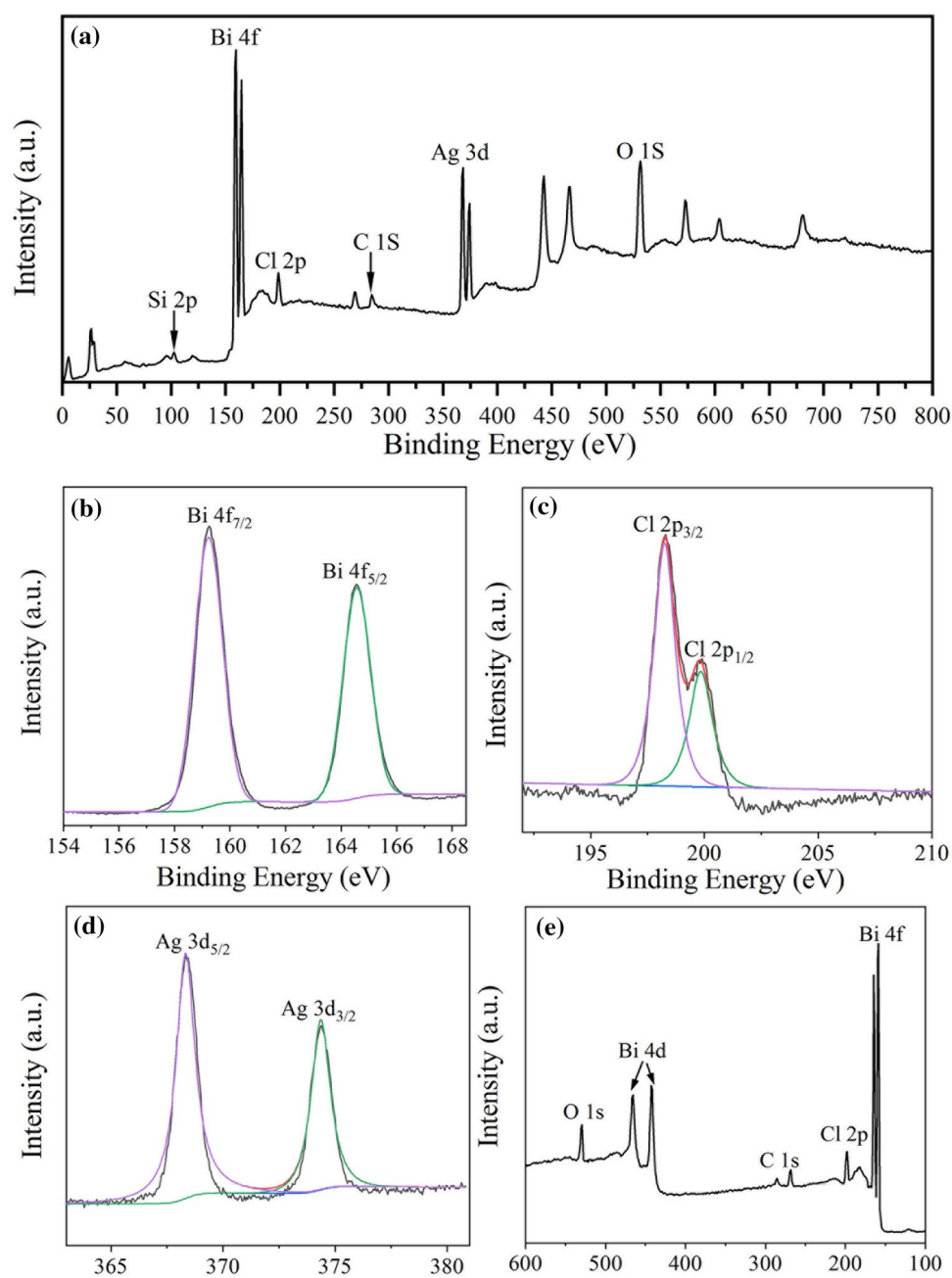
$$E_{\text{VB}} = \chi - E^{\circ} + 0.5E_g \quad (3)$$

where χ is the geometric mean of the electronegativity of the constituent atoms forming the semiconductor, E° is the energy of the free electrons on the hydrogen scale (ca. 4.5 eV), and E_g is the band gap energy of the semiconductor. The χ value for BiOCl was 6.64 eV. From this equation, E_{VB} and E_{CB} of BiOCl were calculated to be 3.49 and 0.78 eV, respectively.

3.1.5 FTIR

The chemical structure and bonding of the samples were further studied by FTIR. All samples showed significant absorption peaks at 1664, 2965, and 3400 cm⁻¹, which may be attributed to the O–H stretch of H₂O adsorbed on the surface of the photocatalyst [40, 41], while the peak at 1374 cm⁻¹ was assigned to the stretching vibrations of the CH₂ groups in ethanol [7]. In the case of Ag₆Si₂O₇ (Fig. 5a), the absorption peaks at 470 and 570 cm⁻¹ may be associated to the bending mode of Si–O–Si, while the vibration band of 987 cm⁻¹ was attributed to the Si–O bending mode [42]. As shown in Fig. 5b, the peak observed at 519 cm⁻¹ was produced by Bi–O stretching vibration [43]. The absorption peaks at 430 and 1050 cm⁻¹ were ascribed to the O–Cl stretching and symmetric stretching vibrations of the Bi–Cl bond, respectively [44, 45], which fully confirmed the composition of the BiOCl photocatalyst. The sharp peaks at 870 cm⁻¹ may

Fig. 3 The XPS spectra of 1/1 BiOCl/Ag₆Si₂O₇ (a); Bi 4f (b); Cl 2p (c); Ag 3d (d) and pure BiOCl (e)



be produced by C–H bond associated with small amounts of ethylene glycol present on the surface of BiOCl. Since BiOCl was tightly encapsulated by Ag₆Si₂O₇, the FTIR spectrum of the BiOCl/Ag₆Si₂O₇ photocatalyst was similar to that of Ag₆Si₂O₇ (Fig. 5c). All the peaks of the BiOCl/Ag₆Si₂O₇ composite photocatalysts revealed the presence of BiOCl and Ag₆Si₂O₇ exclusively. Thus, new phases other than BiOCl and Ag₆Si₂O₇ were not observed, which further demonstrated that the BiOCl/Ag₆Si₂O₇ nanocomposite was successfully synthesized, in line with the XRD and XPS results.

3.2 Photocatalytic Activity

The MO degradation curves on BiOCl, *x* BiOCl/Ag₆Si₂O₇, and Ag₆Si₂O₇ are shown in Fig. 6a. The degradation efficiencies of pure BiOCl and Ag₆Si₂O₇ after 40 min of reaction were 19.0 and 16.0%, respectively. The photocatalytic activity of *x* BiOCl/Ag₆Si₂O₇ towards the degradation of MO showed a maximum for Bi to Ag molar ratio of 1:1 (98.1%) and a decrease thereafter. To the best of our knowledge, the photocatalytic efficiency of this 1/1 BiOCl/Ag₆Si₂O₇ material was much higher than those of

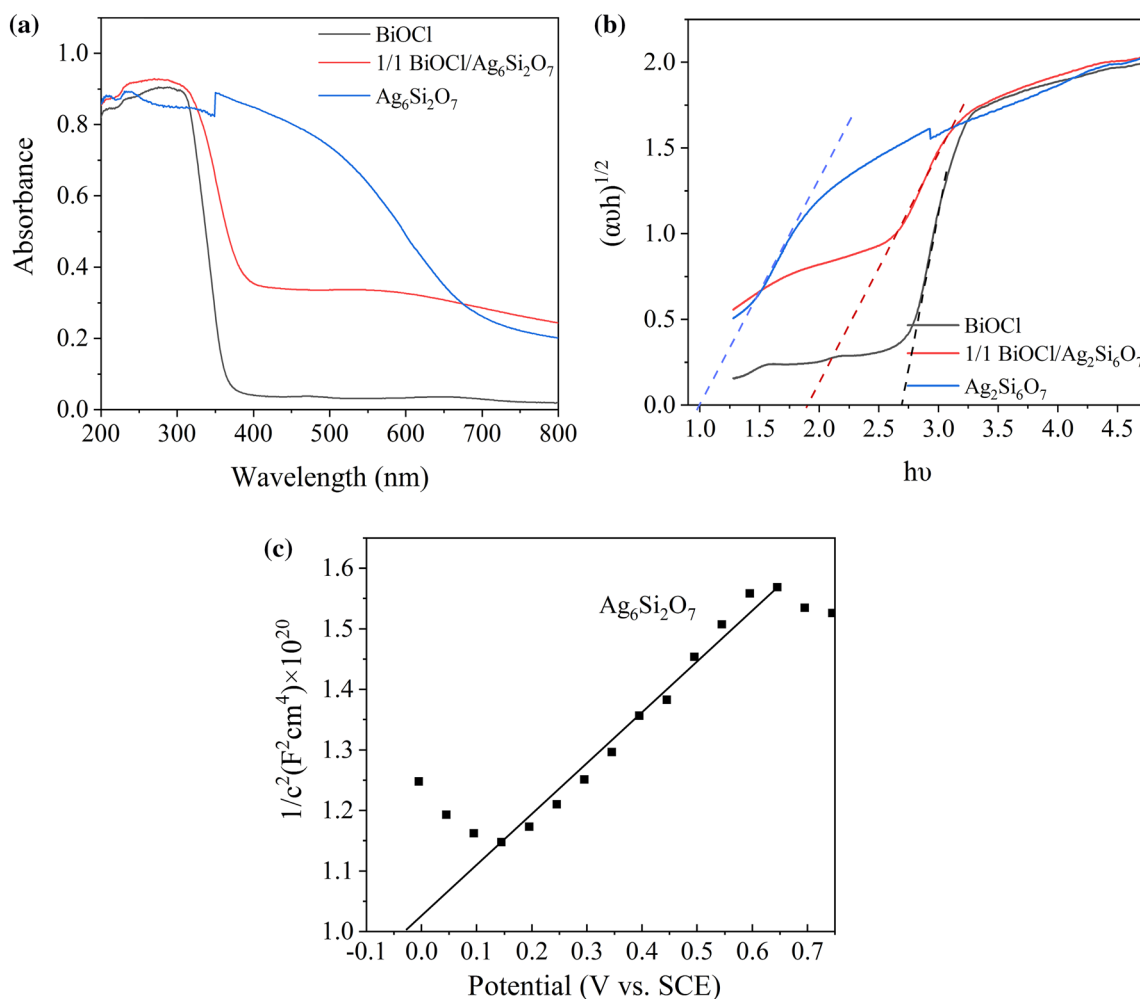


Fig. 4 UV–Vis diffuse reflectance spectra (a); band energy (b) and Mott–Schottky curve (c) of samples

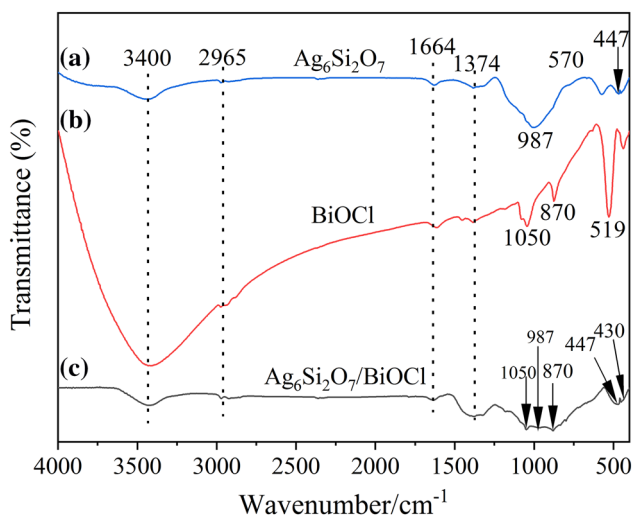


Fig. 5 FT-IR spectra for the Ag₆Si₂O₇ (a); BiOCl (b); and 1/1 BiOCl/Ag₆Si₂O₇ (c) samples

BiOBr/BiPO₄ [46], BiOBr_{0.75}I_{0.25}/BiOIO₃ [47], BiOBr/RGO [48]. In addition, in order to better understand the reaction kinetics of the photocatalytic degradation process of MO, a pseudo-first-order model was applied according to the following equation:

$$\ln(C_0/C) = K_{app}t \tag{4}$$

where C_0 is the initial concentration of MO (mg/L); C is the concentration of MO at a time t (mg/L); t is the irradiation time (min), and K_{app} is the reaction rate constant (1/min). The K_{app} values of the different samples are shown in Fig. 6b. The K_{app} values were calculated to be 0.0710, 0.0211, 0.0170, 0.0041, 0.0032, 0.0047, 0.0024 1/min for the 1/1 BiOCl/Ag₆Si₂O₇, 2/1 BiOCl/Ag₆Si₂O₇, 4/1 BiOCl/Ag₆Si₂O₇, 1/2 BiOCl/Ag₆Si₂O₇, 1/4 BiOCl/Ag₆Si₂O₇, BiOCl and Ag₆Si₂O₇, respectively. Thus, 1/1 BiOCl/Ag₆Si₂O₇ showed the highest K_{app} among the samples tested herein. This value was ca. 15.2 and 29.6 times higher than that of BiOCl and Ag₆Si₂O₇, respectively.

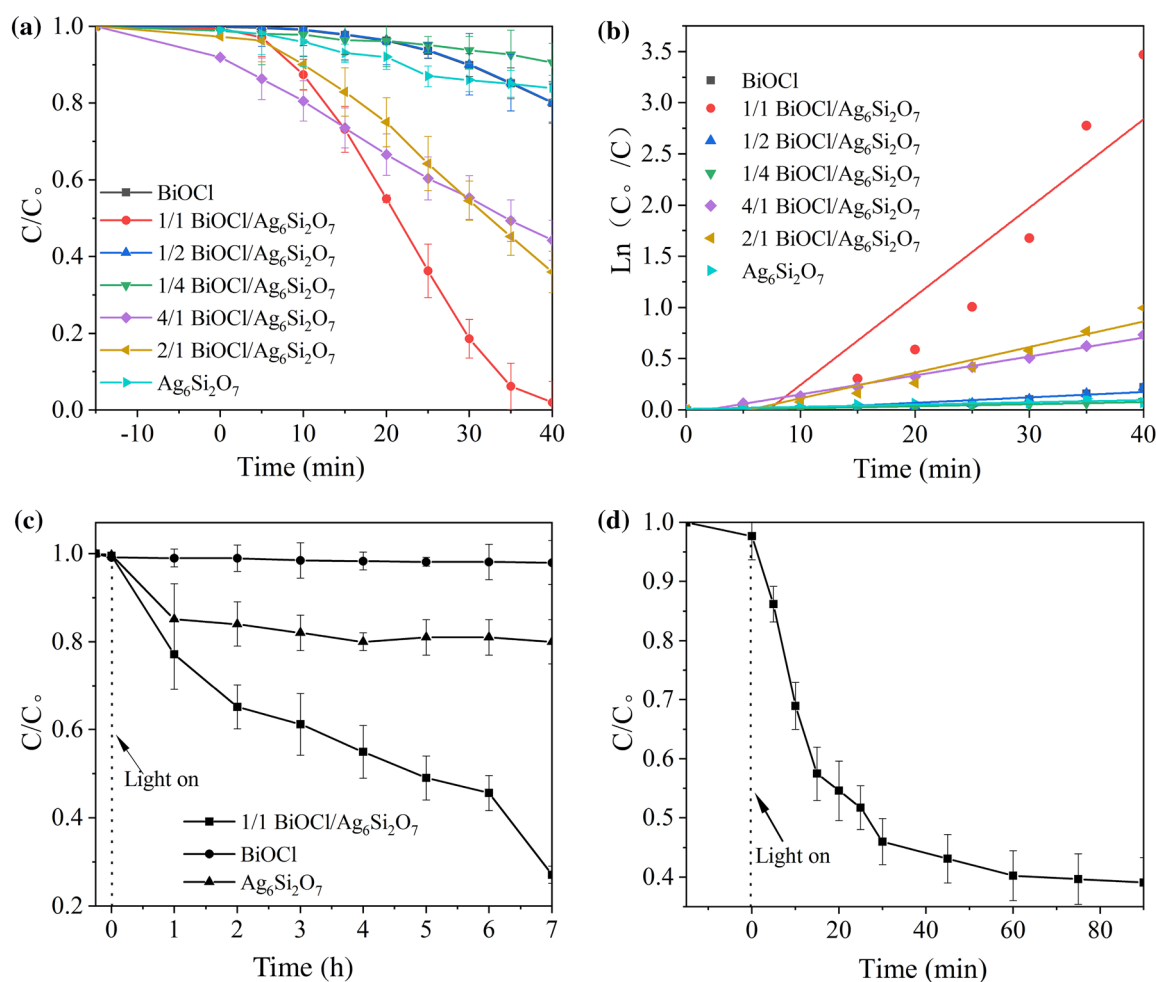


Fig. 6 Photocatalytic activities of the samples towards the MO degradation (a); apparent rate constants for the photocatalytic degradation of MO solution (b); photodegradation curves of phenol over BiOCl,

Ag₆Si₂O₇ and 1/1 BiOCl/Ag₆Si₂O₇ (c); TOC removal on the MO solution in the presence of the 1/1 BiOCl/Ag₆Si₂O₇ catalyst (d)

To eliminate the influence of dye sensitization on the degradation process, we used a colorless and refractory substance such as phenol as the degradation target to further study the photocatalytic activity of BiOCl/Ag₆Si₂O₇. As revealed in Fig. 6c, only 0.3 and 20% of phenol were degraded by BiOCl and Ag₆Si₂O₇ within 7 h, respectively. In contrast, 1/1 BiOCl/Ag₆Si₂O₇ decomposed 83% of phenol within the same time period. The superior photocatalytic activity of 1/1 BiOCl/Ag₆Si₂O₇ originated from a synergistic effect between BiOCl and Ag₆Si₂O₇.

The concentration of total organic carbon (TOC) was selected as the mineralization index to characterize the MO degradation degree. As shown in Fig. 6d, 60.1% of the TOC was mineralized after 90 min under irradiation, revealing that the BiOCl/Ag₆Si₂O₇ nanocomposite has a great potential in environmental remediation and polluted wastewater treatment applications.

3.3 Photocurrent Properties and Stability of BiOCl/Ag₆Si₂O₇

High photocurrent intensities are indicative of high e⁻-h⁺ separation efficiencies, which is related to the photocatalytic performance [49]. Herein, the mechanism governing the generation, separation, and transformation of photogenerated charges was investigated by monitoring the variation of photocurrent time at room temperature. As shown in Fig. 7a, the instantaneous photocurrent of the 1/1 BiOCl/Ag₆Si₂O₇ nanocomposite was ca. 2.5 and 2.6 times higher than those of BiOCl and Ag₆Si₂O₇, respectively. This higher photocurrent of the 1/1 BiOCl/Ag₆Si₂O₇ nanocomposite was attributed to its higher separation efficiency for the photoinduced e⁻ and h⁺ pairs, which resulted in higher photocatalytic activities.

The stability of a photocatalyst is the most important indicator to evaluate its practical applications. We performed

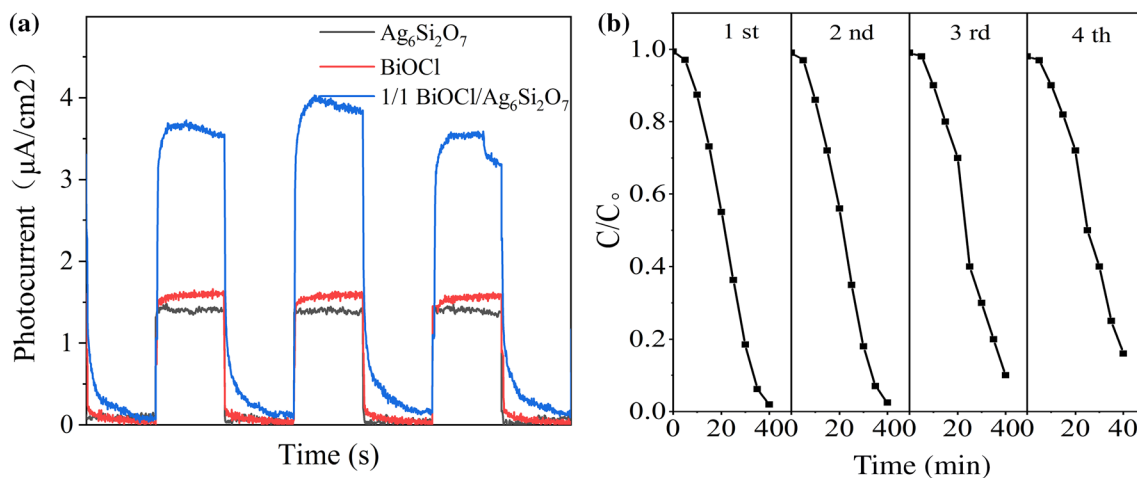


Fig. 7 Transient photocurrent densities of samples (a) and repeated photocatalytic experiments of the 1/1 BiOCl/Ag₆Si₂O₇ nanocomposite under simulated visible light (Catalyst dosage = 1 g/L, C₀ = 10 mg/L) (b)

MO degradation cycling tests on 1/1 BiOCl/Ag₆Si₂O₇ (Fig. 7b). The photocatalytic efficiency of 1/1 BiOCl/Ag₆Si₂O₇ remained unchanged after four successive cycles. This result was in line with the XRD results (Fig. 2d), indicating that the heterojunction photocatalysts was highly stable and possessed high catalytic activity.

3.4 Photocatalytic Mechanism

In order to determine the role of these active substances within the Photodegradation process of MO, three different radical scavengers were added to the reaction system namely, benzoquinone (BQ), ammonium oxalate (AO), and isopropyl alcohol (IPA) as superoxide radical ($\cdot\text{O}_2^-$), hole (h^+), and hydroxyl radical ($\cdot\text{OH}$) scavengers, respectively. As shown in Fig. 8, when IPA was added to the reaction system, the photocatalytic activity of BiOCl/Ag₆Si₂O₇ remained nearly unchanged, indicating that $\cdot\text{OH}$ was not the main active free radical species. However, addition of BQ and AO resulted in significant decreases of the MO degradation efficiency, indicating that h^+ and $\cdot\text{O}_2^-$ were the mainly active species.

Based on the above results, a possible Z-scheme photocatalytic mechanism on the BiOCl/Ag₆Si₂O₇ heterojunction photocatalyst under visible light was proposed (Fig. 9). As is well-known, the Fermi level (EF) of a p-type semiconductor such as BiOCl is close to its VB, while Ag₆Si₂O₇ is an n-type semiconductor and therefore EF is close to its CB. When Ag₆Si₂O₇ photocatalyst grown on the surface of the BiOCl particles and formed a p–n heterojunction, the energy level of BiOCl would shift to higher values. While, the energy level of Ag₆Si₂O₇ would shift continuously downward until the EFs of BiOCl and Ag₆Si₂O₇ reached an equilibrium. At the same time, a strong internal electric field would be also formed between BiOCl and Ag₆Si₂O₇.

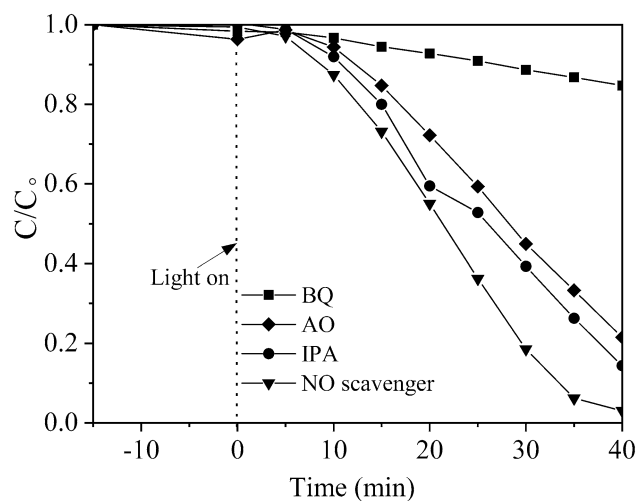


Fig. 8 Reactive species trapping experiments (catalyst dosage = 1 g/L, C₀ = 10 mg/L)

Under visible light irradiation, both BiOCl and Ag₆Si₂O₇ were simultaneously excited to produce h^+ and e^- . Owing to the strong internal electric field in the closely contacted BiOCl and Ag₆Si₂O₇, the photoinduced e^- on the CB of Ag₆Si₂O₇ was transferred to the VB of BiOCl. We speculated that, at this moment, the E_{CB} of BiOCl was more negative than the standard oxygen reduction potential (-0.33 eV vs. NHE) [50]. Therefore, it was possible for the photogenerated electrons in the CB of BiOCl to reduce O₂ to $\cdot\text{O}_2^-$. Although, the h^+ produced in the VB of Ag₆Si₂O₇ may become more positive, the E_{CB} of Ag₆Si₂O₇ was below the standard redox potential of $\text{OH}^-/\cdot\text{OH}$ (2.38 eV) [51]. Thus, $\cdot\text{OH}$ species were not detected in the active substance capture experiment. However, owing to their superior oxidizing power, the

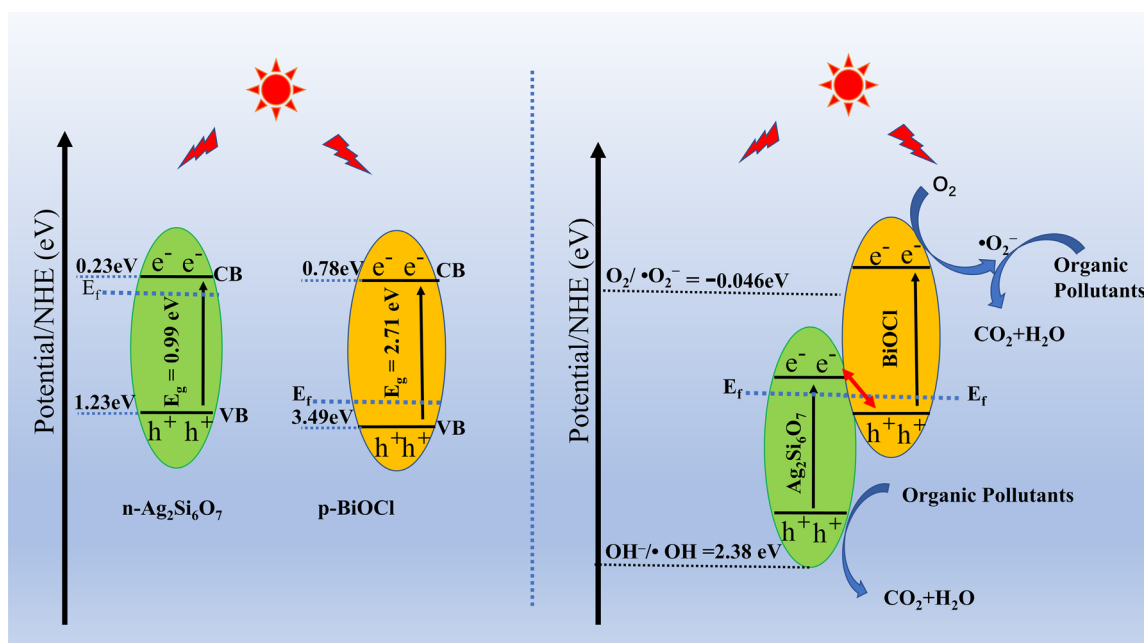


Fig. 9 Z-scheme photocatalytic mechanism of the of the BiOCl/Ag₆Si₂O₇ photocatalyst

h^+ produced in the VB of Ag₆Si₂O₇ could directly oxidize the organic contaminants to form CO₂ and H₂O. According to recent literature, partial chloride ions were oxidized to chlorine in the composite photocatalyst containing chloride ions during the photocatalytic process. Therefore, we inferred that in this reaction system, the chlorine molecules adsorbed on BiOCl/Ag₆Si₂O₇ could directly oxidize MO or phenol and returned to the original ionic state (Cl⁻) due to their superior oxidation capacity. In summary, these excellent optical absorption properties and rapid photo-generated charge transfer rates led to the high photocatalytic activity for the BiOCl/Ag₆Si₂O₇ heterojunction photocatalyst.

3.5 Degradation Pathway of MO

In order to better understand the degradation pathway of MO in the photocatalytic process, we conducted GC-MS analysis of the intermediate products of reaction, and proposed a reasonable degradation pathway (Fig. 10). The main intermediate products were benzenesulfonic acid with retention time (RT) 8.75 min and 2-methyl-*N*-phenyl with RT of 8.77 min. These substances were the initial degradation products of MO and revealed that the catalytic process started with the cleavage of the azo group linking the two aromatic rings. Longer irradiation times resulted in the onset of new intermediates (benzene with a RT of 12.21 min and aniline with a RT of 12.29 min), which were degraded to heptane. Finally,

these small molecular organics were oxidized to H₂O and CO₂.

4 Conclusions

In summary, a novel BiOCl/Ag₆Si₂O₇ p-n heterojunction nanocomposite was successfully prepared by a deposition-precipitation method at room temperature. Various characterization techniques were used to study the structure, morphology, and optical properties of these heterojunctions. Among the samples tested, the 1/1 BiOCl/Ag₆Si₂O₇ p-n heterojunction exhibited the highest photocatalytic activity towards the degradation of different organic (MO and phenol) degradation under visible light irradiation. This enhanced photoactivity was attributed to the intimate p-n heterostructure formed between BiOCl and Ag₆Si₂O₇, which promoted significantly efficient separation and transfer of photogenerated charge carriers and thereby inhibited charge-carrier recombination. Simultaneously, the materials displayed good stability and recyclability. It was noteworthy that this is the first report on photocatalytic decomposition of organic compounds over BiOCl/Ag₆Si₂O₇ nanocomposites under visible light condition. We believe that these results will encourage further investigations and the development of p-n BiOCl/Ag₆Si₂O₇ heterojunction nanocomposites for refractory polluted wastewater applications.

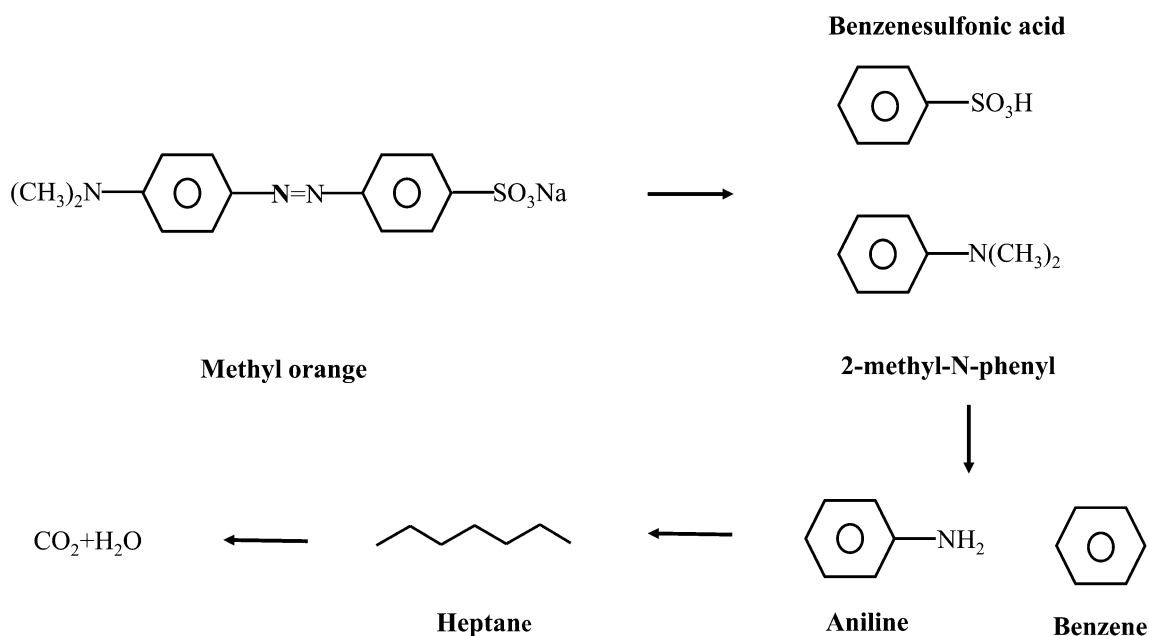


Fig. 10 Degradation pathway proposed on the basis of GC/MS analysis during photodegradation of MO

Acknowledgements The authors acknowledge financial support from the National Natural Science Foundation of China (NSFC) (Nos. 20407129, 51578519), Major Science and Technology Program for Water Pollution Control and Treatment (No. 2017ZX07202002) and the Fundamental Research Funds for the Central Universities (No. 2652017190).

References

- Lin X, Xi Y, Zhao R et al (2017) Construction of C60-decorated SWCNTs (C60-CNTs)/bismuth-based oxide ternary heterostructures with enhanced photocatalytic activity. *RSC Adv* 7:53847–53854
- Lv D, Zhang D, Pu X et al (2017) One-pot combustion synthesis of BiVO₄/BiOCl composites with enhanced visible-light photocatalytic properties. *Sep Purif Technol* 174:97–103
- Lin X, Xu D, Zhao R et al (2017) Highly efficient photocatalytic activity of g-C₃N₄ quantum dots (CNQDs)/Ag/Bi₂MoO₆ nanoheterostructure under visible light. *Sep Purif Technol* 178:163–168
- Chen X, Chen X, Wang X, Tingzhen LI (2018) Preparation of Nd-Er/ZnO-TiO₂ photocatalyst and its photocatalytic degradation effect on acid magenta. *Ecol Environ Monitor Three Gorges* 3:41–46
- Diazdemera Y, Aranda A, Bracco L et al (2017) Formation of secondary organic aerosols from the ozonolysis of dihydrofurans. *Atmos Chem Phys* 17:1–18. <https://doi.org/10.5194/acp-17-2347-2017>
- Kaur A, Kansal SK (2016) Bi₂WO₆ nanocuboids: an efficient visible light active photocatalyst for the degradation of levofloxacin drug in aqueous phase. *Chem Eng J* 302:194–203
- Lin X, Xu D, Jiang S et al (2017) Graphitic carbon nitride nanocrystals decorated AgVO₃ nanowires with enhanced visible-light photocatalytic activity. *Catal Commun* 89:96–99
- Fu Y, Liu C, Zhu C et al (2018) High-performance NiO/g-C₃N₄ composites for visible-light-driven photocatalytic overall water splitting. *Inorg Chem Front* 106:409–417
- Akimov AV, Neukirch AJ, Prezhdo OV (2013) ChemInform abstract: theoretical insights into photoinduced charge transfer and catalysis at oxide interfaces. *Chem Rev* 113:4496–4565
- Bing Y, Li Q, Iwai H et al (2011) Hydrogen production using zinc-doped carbon nitride catalyst irradiated with visible light. *Sci Technol Adv Mater* 12:034401
- Wang X, Chen X, Thomas A et al (2010) Metal-containing carbon nitride compounds: a new functional organic–metal hybrid material. *Adv Mater* 21:1609–1612
- Liu Q, Zhang J (2013) Graphene supported Co-g-C₃N₄ as a novel metal–macrocylic electrocatalyst for the oxygen reduction reaction in fuel cells. *Langmuir* 29:3821–3828
- Zhang W, Wang Y, Wang Z et al (2010) Highly efficient and noble metal-free NiS/CdS photocatalysts for H₂ evolution from lactic acid sacrificial solution under visible light. *Chem Commun* 46:7631–7633
- Yang G, Ding H, Chen D et al (2018) Construction of urchin-like ZnIn₂S₄-Au-TiO₂ heterostructure with enhanced activity for photocatalytic hydrogen evolution. *Appl Catal B* 234:260–267
- Ye L, Liu J, Jiang Z et al (2013) Facets coupling of BiOBr-g-C₃N₄ composite photocatalyst for enhanced visible-light-driven photocatalytic activity. *Appl Catal B* 142–143:1–7
- Cao J, Xu B, Luo B et al (2011) Novel BiOI/BiOBr heterojunction photocatalysts with enhanced visible light photocatalytic properties. *Catal Commun* 13:63–68
- Lin X, Xu D, Xi Y et al (2017) Construction of leaf-like g-C₃N₄/Ag/BiVO₄ nanoheterostructures with enhanced photocatalysis performance under visible-light irradiation. *Colloids Surf A* 513:117–124
- Malligavathy M, Padiyan DP (2018) Phase purity analysis and optical studies of Bi₂O₃ nanoparticles suitable for photocatalytic activity. *Int J Nanosci* 17(3):1760040

19. Li Y, Liu J, Huang X, Li G (2007) Hydrothermal synthesis of Bi_2WO_6 uniform hierarchical microspheres. *Cryst Growth Des* 7:1350–1355
20. Dunkle SS, Helmich RJ, Suslick KS (2009) BiVO_4 as a visible-light photocatalyst prepared by ultrasonic spray pyrolysis. *J Phys Chem C* 113:11980–11983
21. Zou ZG, Ye JH, Arakawa H (2001) Substitution effects of In^{3+} by Fe^{3+} on photocatalytic and structural properties of $\text{Bi}_2\text{InNbO}_7$ photocatalysts. *J Mol Catal A* 168:289–297
22. Henle J, Simon P, Frenzel A et al (2007) Nanosized BiOX ($X = \text{Cl}, \text{Br}, \text{I}$) particles synthesized in reverse microemulsions. *Chem Mater* 19:366–373
23. Cao J, Xu B, Lin H et al (2012) Novel Bi_2S_3 -sensitized BiOCl with highly visible light photocatalytic activity for the removal of rhodamine B. *Catal Commun* 26:204–208
24. Peng H, Chan CK, Meister S et al (2015) Shape evolution of layer-structure bismuth oxychloride nanostructures via low-temperature chemical vapor transport. *Chem Mater* 21:247–252
25. Duo F, Wang Y, Mao X et al (2015) A $\text{BiPO}_4/\text{BiOCl}$ heterojunction photocatalyst with enhanced electron-hole separation and excellent photocatalytic performance. *Appl Surf Sci* 340:35–42
26. Zuo Y, Wang C, Sun Y, Cheng J (2015) Preparation and photocatalytic properties of $\text{BiOCl}/\text{Bi}_2\text{MoO}_6$ composite photocatalyst. *Mater Lett* 139:149–152
27. Xie T, Xu L, Liu C et al (2014) Magnetic composite $\text{BiOCl}-\text{SrFe}_{12}\text{O}_{19}$: a novel p-n type heterojunction with enhanced photocatalytic activity. *Dalton Trans* 43:2211–2220
28. Wang XJ, Wang Q, Li FT et al (2013) Novel $\text{BiOCl}-\text{C}_3\text{N}_4$ heterojunction photocatalysts: In situ preparation via an ionic-liquid-assisted solvent-thermal route and their visible-light photocatalytic activities. *Chem Eng J* 234:361–371
29. Chen H, Chen N, Gao Y, Feng C (2018) Photocatalytic degradation of methylene blue by magnetically recoverable $\text{Fe}_3\text{O}_4/\text{Ag}_6\text{Si}_2\text{O}_7$ under simulated visible light. *Powder Technol* 326:247–254
30. Qin J, Chen N, Feng C et al (2018) Fabrication of a narrow-band-gap $\text{Ag}_6\text{Si}_2\text{O}_7/\text{BiOBr}$ composite with high stability and enhanced visible-light photocatalytic activity. *Catal Lett* 148:2777–2788
31. Lou Z, Huang B, Wang Z et al (2015) $\text{Ag}_6\text{Si}_2\text{O}_7$: a silicate photocatalyst for the visible region. *Cheminform* 45:3873–3875. <https://doi.org/10.1021/cm500657n>
32. He Z, Shi Y, Gao C et al (2014) $\text{BiOCl}/\text{BiVO}_4$ p-n heterojunction with enhanced photocatalytic activity under visible-light irradiation. *J Phys Chem C* 118:389–398
33. Chen H, Chen N, Feng C, Gao Y (2018) Synthesis of a novel narrow-band-gap iron(II,III) oxide/titania/silver silicate nanocomposite as a highly efficient and stable visible light-driven photocatalyst. *J Colloid Interface Sci* 515:119–128
34. Shi L, Ma J, Yao L et al (2018) Enhanced photocatalytic activity of $\text{Bi}_{12}\text{O}_{17}\text{Cl}_2$ nano-sheets via surface modification of carbon nanotubes as electron carriers. *J Colloid Interface Sci* 519:1293–301
35. Ai Z, Ho W, Lee S, Zhang L (2009) Efficient photocatalytic removal of NO in indoor air with hierarchical bismuth oxybromide nanoplate microspheres under visible light. *Environ Sci Technol* 43:4143–4150
36. Mehraj O, Mir NA, Pirzada BM et al (2014) In-situ anion exchange synthesis of $\text{AgBr}/\text{Ag}_2\text{CO}_3$ hybrids with enhanced visible light photocatalytic activity and improved stability. *J Mol Catal A* 395:16–24
37. Shang J, Hao W, Lv X et al (2014) Bismuth oxybromide with reasonable photocatalytic reduction activity under visible light. *ACS Catal* 4:954–961
38. Xiao X, Jiang J, Zhang L (2013) Selective oxidation of benzyl alcohol into benzaldehyde over semiconductors under visible light: the case of $\text{Bi}_{12}\text{O}_{17}\text{Cl}_2$ nanobelts. *Appl Catal B* 142–143:487–493
39. Li Y, Wang J, Yao H et al (2011) Efficient decomposition of organic compounds and reaction mechanism with BiOI photocatalyst under visible light irradiation. *J Mol Catal A* 334:116–122
40. Ma J, Ding J, Yu L et al (2015) BiOCl dispersed on NiFe-LDH leads to enhanced photo-degradation of Rhodamine B dye. *Appl Clay Sci* 109–110:76–82
41. Pirhashemi M, Habibi-Yangjeh A (2017) Ultrasonic-assisted preparation of plasmonic $\text{ZnO}/\text{Ag}/\text{Ag}_2\text{WO}_4$ nanocomposites with high visible-light photocatalytic performance for degradation of organic pollutants. *J Colloid Interface Sci* 491:216–229
42. Sahu IP, Bisen DP, Brahma N (2015) Luminescence properties of green emitting $\text{Ca}_2\text{MgSi}_2\text{O}_7:\text{Eu}^{2+}$ phosphor by solid state reaction method. *Phys Proc* 76:80–85
43. Nayak MC, Isloor AM, Moslehyani A, Ismail AF (2017) Preparation and characterization of PPSU membranes with BiOCl nanowafers loaded on activated charcoal for oil in water separation. *J Taiwan Inst Chem Eng* 77:293–301
44. Tripathi GK, Kurchania R (2016) Effect of doping on structural, optical and photocatalytic properties of bismuth oxychloride nanomaterials. *J Mater Sci Mater Electron* 27:5079–5088
45. Yang Q, Zhai Y, Li X, Li H (2018) Synthesis of $\text{Fe}_3\text{O}_4/\text{Pr-BiOCl}$ /Luffa composites with enhanced visible light photoactivity for organic dyes degradation. *Mater Res Bull* 106:409–417
46. Jia X, Cao J, Lin H et al (2016) Novel I- $\text{BiOBr}/\text{BiPO}_4$ heterostructure: synergetic effects of I-ion doping and the electron trapping role of wide-band-gap BiPO_4 nanorods. *RSC Adv* 6:55755–55763
47. Zeng C, Hu Y, Huang H (2017) $\text{BiOBr}_{0.75}\text{I}_{0.25}/\text{BiOIO}_3$ as a novel heterojunctional photocatalyst with superior visible-light-driven photocatalytic activity in removing diverse industrial pollutants. *ACS Sustain Chem Eng* 5:3897–3905
48. Vadivel S, Keerthi P, Vanitha M et al (2014) Solvothermal synthesis of Sm-doped BiOBr/RGO composite as an efficient photocatalytic material for methyl orange degradation. *Mater Lett* 128:287–290
49. Li T, He Y, Lin H et al (2013) Synthesis, characterization and photocatalytic activity of visible-light plasmonic photocatalyst AgBr-SmVO_4 . *Appl Catal B* 138:95–103
50. Kim J, Lee CW, Choi W (2010) Platinized WO_3 as an environmental photocatalyst that generates OH radicals under visible light. *Environ Sci Technol* 44:6849–6854
51. Cao J, Xu B, Luo B et al (2011) Preparation, characterization and visible-light photocatalytic activity of $\text{AgI}/\text{AgCl}/\text{TiO}_2$. *Appl Surf Sci* 257:7083–7089

Affiliations

Jibo Qin¹ · Nan Chen¹ · Chuanping Feng¹ · Huiping Chen¹ · Zhengyuan Feng¹ · Yu Gao² · Zhenya Zhang³

✉ Nan Chen
chennan@cugb.edu.cn

¹ School of Water Resources and Environment, MOE Key Laboratory of Groundwater Circulation and Environmental Evolution, China University of Geosciences (Beijing), Beijing 100083, People's Republic of China

² College of Chemical and Environmental Engineering, Shandong University of Science and Technology, Qingdao 266590, People's Republic of China

³ Graduate School of Life and Environmental Sciences, University of Tsukuba, 1-1-1 Tennodai, Tsukuba, Ibaraki 305-8572, Japan